8-2010

AFM study of ridges in few-layer epitaxial graphene grown on the carbon-face of 4H-SiC(000(1)over-bar)

Gyan Prakash
Purdue University - Main Campus, gprakash@purdue.edu

Michael A. Capano
Birck Nanotechnology Center, Purdue University, capano@purdue.edu

Michael Bolen
Purdue University, mbolen@purdue.edu

Dmitry Zemlyanov
Birck Nanotechnology Center, Purdue University, dimazemlyanov@purdue.edu

R. Reifenberger
Birck Nanotechnology Center, Purdue University, reifenbr@purdue.edu

Prakash, Gyan; Capano, Michael A.; Bolen, Michael; Zemlyanov, Dmitry; and Reifenberger, R., "AFM study of ridges in few-layer epitaxial graphene grown on the carbon-face of 4H-SiC(000(1)over-bar)" (2010). *Birck and NCN Publications.* Paper 671.
http://dx.doi.org/10.1016/j.carbon.2010.02.026

CARBON 48 (2010) 2383–2393

available at www.sciencedirect.com

ScienceDirect

journal homepage: www.elsevier.com/locate/carbon

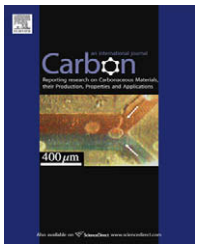

AFM study of ridges in few-layer epitaxial graphene grown on the carbon-face of 4H–SiC(000$\bar{1}$)

Gyan Prakash [a,b,*], *Michael A. Capano* [b,c], *Michael L. Bolen* [b,c], *Dmitry Zemlyanov* [b], *Ronald G. Reifenberger* [a,b]

[a] *Department of Physics, Purdue University, 525 Northwestern Avenue, West Lafayette, IN 47907, USA*
[b] *Birck Nanotechnology Center, Purdue University, 1205 W State Street, West Lafayette, IN 47907, USA*
[c] *School Electrical Engineering, Purdue University, 465 Northwestern Avenue, West Lafayette, IN 47907, USA*

ARTICLE INFO

Article history:
Received 23 November 2009
Accepted 16 February 2010
Available online 19 February 2010

ABSTRACT

A characterization of the graphitic overlayer that forms on 4H–SiC(000$\bar{1}$) substrates heated for ten minutes to temperatures $T > 1350$ °C under vacuum conditions has been performed. X-ray photoelectron spectroscopy of the C-face reveals the presence of graphitic carbon with a thickness that increases with growth temperature. Parallel atomic force microscope (AFM) studies find a mesh-like network of ridges with high curvature that bound atomically flat, tile-like facets of few-layer graphene (FLG). By imaging the network that develops on FLG, it is possible to map out the regions where the elastic energy is concentrated.

1. Introduction

High quality graphene consisting of a single layer of carbon atoms arranged in a dense honeycomb lattice structure has many unique electronic properties that are of considerable current interest [1,2]. Two-dimensional (2D) graphene offers a promise for THz nanoelectronic devices because of the high theoretical electron mobility that is ~10 times greater than observed in Si. Experiments have measured mobilities between 3000 and 27,000 $cm^2/(V\,s)$ [3,4]. Reports of graphene field effect transistors (FETs) have appeared [3–7], including transistor action in the GHz range [8].

Various methods including micro-mechanical cleavage, chemical exfoliation and epitaxial growth have been proposed to prepare few-layer graphene (FLG) [3,9,10]. The difficulty in scaling a mechanical cleavage process to produce large area wafers of graphene has only recently been addressed using transfer-printing techniques [11]. The epitaxial approach is promising because it may produce wafer-scale graphene by simply heating a substrate exhibiting a tendency toward graphitization. Indeed, the preferential sublimation of Si atoms from a SiC substrate [9,12,13] offers an appealing way to grow FLG on wafer-size substrates, but the optimal growth conditions have not yet been identified.

The structural characterization of FLG on SiC has been studied by a variety of surface science techniques such as low energy electron microscopy (LEEM) [14,15], X-ray photoelectron spectroscopy (XPS) [16,17], Raman spectroscopy [18,19], and scanning probe microscopy (SPM) [20,21].

Recent molecular dynamic (MD) simulations [22] of the growth of graphene on 6H–SiC(0001) (Si-face) suggest that the formation of continuous layers of graphene depends on the number of SiC bilayers sublimated. Simulations have shown that sublimation of a single bilayer of SiC produces isolated chain-like and ring-like graphitic structures, two bilayers of SiC are required to produce large graphene-like clusters, and four bilayers are required to form two graphene sheets. Taken together, the MD simulations emphasize the importance of identifying the optimal growth conditions to grow high quality graphene layers.

* *Corresponding author:* Address: Department of Physics, Purdue University, 525 Northwestern Avenue, West Lafayette, IN 47907, USA. Fax: +1 765 494 0706.
E-mail address: gprakash@purdue.edu (G. Prakash).
0008-6223/$ - see front matter
doi:10.1016/j.carbon.2010.02.026

We have performed a systematic study of the graphitic material grown on the C-face of 4H–SiC(000$\bar{1}$) over a range of growth temperatures. For all growth temperatures that produce a continuous layer of graphitization, we find atomically smooth, tile-like facets of FLG bounded by an interlocking mesh of ridge-like surface features. We infer that the mesh-like network forms to minimize the elastic strain energy. Due to the high radius of curvature associated with the ridges, the likelihood of reactive sites that promote chemical reactions increases. As a result, it seems possible that FLG decorated with ridge-like networks will degrade with time, especially if stored under ambient conditions.

We summarize the main results of our study of FLG growth on 4H–SiC(000$\bar{1}$) using primarily XPS and atomic force microscopy (AFM) techniques. In what follows, we do not focus on the complex set of reconstructions that may occur in the restructured interfacial layer that forms on the C-face of SiC, but rather choose to study primarily the graphitic layers that form at growth temperatures greater than 1475 °C.

2. Experimental techniques

2.1. Sample preparation

The SiC substrates used in this study are three inch diam. 4H–SiC(000$\bar{1}$) semi-insulating substrates obtained from CREE with a nominal off-cut angle of 0°. The as-received SiC wafers were chemo-mechanically polished by NovaSiC. After dicing the polished wafer into 1 cm × 1 cm samples, the individual SiC samples are solvent cleaned and then etched in a piranha solution to remove hydrocarbon contamination. Before carbon growth, the samples are subjected to a hydrogen etching at 1500 °C for 10 min. in an Epigress VP508 SiC hot-wall chemical vapor deposition (CVD) reactor. After cooling below 700 °C, the chamber is pumped until the pressure is reduced to $\sim 4 \times 10^{-6}$ mbar. Subsequently, the temperature of the SiC is ramped to a pre-set growth temperature. Typically, the growth pressure is $\sim 5 \times 10^{-5}$ mbar. The temperatures reported in this study are measured using a Heitronics KT81R two-color rationing pyrometer (spectral bands 0.7 and 1.2 μm) with a calibration traceable to the melting temperature of Si at 1410 °C.

In this study, growth times of FLG at a fixed growth temperature are held constant at 10 min. Graphene growth temperatures investigated ranged from 1350 to 1600 °C. After carbon growth for 10 min, the power to the RF generator was shut off and the sample was allowed to cool to room temperature. The temperature during cool down as a function of time t (in s) is well described by the equation $T(t) = T_G\, e^{-\lambda t}$ where T_G is the growth temperature and $\lambda \simeq 8.2 \times 10^{-4}\ s^{-1}$.

2.2. Atomic force microscopy (AFM)

A Nanotec Electronica atomic force microscope was used to image the graphene grown on SiC substrates. AFM images were obtained in intermittent contact mode with a set-point amplitude reduction ratio ($\mathscr{A}/\mathscr{A}_0$) of 0.80, where $\mathscr{A}_0 = 35$ nm is the free vibration amplitude and $\mathscr{A}$ is the set-point amplitude. The AFM studies were performed under ambient conditions. The z-axis of the AFM was calibrated against the step height of highly oriented pyrolytic graphite (HOPG). The x, y calibrations were performed using a Micromasch (Model-TGZ01) xyz calibration grating. WSxM software was used to both acquire and analyze the images [23]. The microcantilevers used in this study were purchased from Nanosensor (Model SSS-NCL-10) and have a nominal resonance frequency of 190 kHz, a nominal spring constant of 48 N/m, and a typical tip radius of 2 nm. The guaranteed tip radius of curvature is specified to be less than 5 nm with a yield >80%. For each sample studied, we typically reposition the tip ~5 times by a few millimeters to several random locations to obtain many images of the substrate. No significant changes in the AFM images have been observed from location to location. Unless otherwise stated all AFM images contain 256 × 256 pixels.

2.3. X-ray photoelectron spectroscopy

As in previous studies [21], XPS provided a non-intrusive tool to investigate the chemical nature of the graphitized surface and also provided estimates for the thickness of the FLG. The XPS data were obtained with a Kratos Ultra DLD spectrometer using monochromatic Al Kα radiation ($h\nu$ = 1486.58 eV). Survey and high-resolution spectra were collected at fixed analyzer pass energies of 160 and 20 eV, respectively. Binding energy (BE) values refer to the Fermi edge and the energy scale was calibrated using Au $4f_{7/2}$ at 84.0 eV and Cu $2p_{3/2}$ = 932.67 eV. Typically, FLG samples were sufficiently good conductors that no charge reference was required. The C 1s peak from graphitic carbon was observed at 284.5 eV. The conductivity of a pure SiC substrate was not high enough and therefore a commercial Kratos charge neutralizer was used. The charge reference was the Si $2p_{3/2}$ peak at 100.5 eV. The data were analyzed with commercially available software, CasaXPS (version 2313Dev64). The individual peaks were fitted by a Gaussian–Lorentzian function after linear or Shirley type background subtraction.

3. XPS results

Analysis of the C 1s core level region allowed a convenient comparison between a reference HOPG samples and graphene–SiC samples grown at 1475, 1500 and 1550 °C. Data from an unannealed carbon face of 4H–SiC substrate are also included. The XPS spectra from both HOPG and the three graphene–SiC samples are plotted in Fig. 1. The XPS spectrum from HOPG shows a peak near 284.5 eV; this peak is indicative of sp^2 hybridized C–C bonds which characterize graphitic carbon. A strong peak near 284.5 eV was observed on the samples heated to different temperatures (Fig. 1) confirming that thin layers of sp^2 hybridized C atoms are present across the SiC substrate for all growth temperatures studied. As the growth temperature increases, the contribution of the C–Si component is attenuated due to the increasing thickness of the graphitic overlayer.

The number of photoelectrons collected from a semi-infinite SiC sample at a photoemission angle θ measured from the normal can be written as [21,24]

$$N_{SiC}(\theta) = \Omega_0(E_{SiC}) A_0(E_{SiC}) D_0(E_{SiC}) \rho_{SiC} \frac{d\sigma(\text{C 1s})}{d\Omega} \Lambda^{SiC}(E_{SiC}) \cos\theta \quad (1)$$

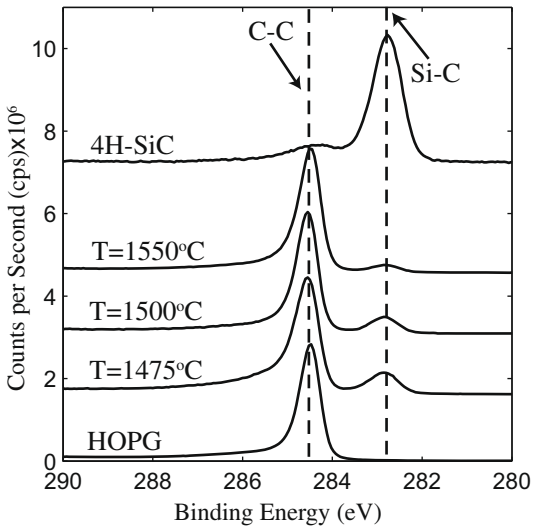

Fig. 1 – Comparison of the C 1s spectra taken from different samples at 0° photoemission angle. The XPS spectrum from HOPG identifies the binding energy of the sp^2 C–C bond XPS spectrum. Data for FLG grown for ten minutes at temperatures of 1475, 1500, and 1550 °C show a reduced C–Si signal as the FLG thickness increases. A representative C 1s spectrum from SiC is also provided. Each spectrum is shifted upward by a constant offset for purposes of clarity.

where $N_{SiC}(\theta)$ is the area under the C 1s peak of SiC, E_{SiC} is the kinetic energy of the C 1s photoelectrons originating from the SiC substrate, Ω_0 is the acceptance solid angle of the energy analyzer; A_0 is the effective sample area, D_0 is the instrument detection efficiency; $d\sigma/d\Omega$ is the differential cross-section for the photoemission process, $\Lambda^{SiC}(E_{SiC})$ is the attenuation length of the photoelectrons with kinetic energy of E_{SiC}, and ρ_{SiC} is the density of the SiC substrate in atoms/cm^3. If a graphitic overlayer of thickness t is placed on top of the SiC, then Eq. (1) must be modified to account for attenuation by the overlayer as

$$N_{SiC}(\theta) = \Omega_0(E_{SiC})A_0(E_{SiC})D_0(E_{SiC})\rho_{SiC}\frac{d\sigma(\text{C 1s})}{d\Omega}\Lambda^{SiC}(E_{SiC}) \times \cos\theta\, e^{-\left(\frac{t}{\Lambda^G(E_{SiC})\cos\theta}\right)} \quad (2)$$

The number of photoelectrons collected from a semi-infinite graphene sample at a photoemission angle θ measured from the normal can be written as

$$N_G(\theta) = \Omega_0(E_G)A_0(E_G)D_0(E_G)\rho_G\frac{d\sigma(\text{C 1s})}{d\Omega}\Lambda^G(E_G)\cos\theta \quad (3)$$

where the symbols represent the same quantities as defined in Eq. (1) while the subscript/superscript G denotes photoelectrons from graphene rather than SiC. If the graphene sample has a finite thickness t, the number of photoelectrons emitted will be

$$N_G(\theta) = \Omega_0(E_G)A_0(E_G)D_0(E_G)\rho_G\frac{d\sigma(\text{C 1s})}{d\Omega}\Lambda^G(E_G) \times \cos\theta\left[1 - e^{-\left(\frac{t}{\Lambda^G(E_G)\cos\theta}\right)}\right] \quad (4)$$

The kinetic energies of the C 1s photoelectrons originating from SiC and graphene are nearly identical so, $E_G \approx E_{SiC} \equiv E_{C1s}$ = 1201 eV [25] and therefore attenuation lengths should be the same, $\Lambda^G(E_G) \approx \Lambda^G(E_{SiC}) \equiv \Lambda^G(E_{C1s})$. This allows the ratio of the graphene C 1s photoemission peak to the SiC C 1s signal to be written as

$$\frac{N_G(\theta)}{N_{SiC}(\theta)} = \frac{\rho_G\Lambda^G(E_{C1s})\left[1 - e^{-\left(\frac{t}{\Lambda^G(E_{C1s})\cos\theta}\right)}\right]}{\rho_{SiC}\Lambda^{SiC}(E_{C1s})\, e^{-\left(\frac{t}{\Lambda^G(E_{C1s})\cos\theta}\right)}} \quad (5)$$

The ratio $N_G(\theta)/N_{SiC}(\theta)$ can be accurately measured using curve-fitting of the C 1s spectrum with two components (C–C and Si–C) and this ratio can then be used to calculate the thickness t of the graphene overlayer. Taking the natural log of both sides of Eq. (5) and rearranging terms yields,

$$\ln\left(\frac{N_G(\theta)}{N_{SiC}(\theta)}\frac{\rho_{SiC}}{\rho_G}\frac{\Lambda^{SiC}(E_{C1s})}{\Lambda^G(E_{C1s})} + 1\right) = \frac{t}{\Lambda^G(E_{C1s})}\frac{1}{\cos\theta} \quad (6)$$

The slope of a linear least-squares fit of $\ln\left(\frac{N_G(\theta)}{N_{SiC}(\theta)}\frac{\rho_{SiC}}{\rho_G}\frac{\Lambda^{SiC}(E_{C1s})}{\Lambda^G(E_{C1s})} + 1\right)$ versus $1/\cos\theta$ is equal to the ratio $\frac{t}{\Lambda^G(E_{C1s})}$. This formalism is discussed in more detail in the Supporting Information provided in Ref. [21].

The ratio $N_G(\theta)/N_{SiC}(\theta)$ was measured over a range of photoemission angles θ ranging between 0° and 60° and a least-squares fit to Eq. (6) allowed an estimate of t, the thickness of the carbon overlayer. The results are summarized in Table 1. Because of the finite diameter of the XPS analysis spot, an estimate of the thickness represents an average value characterizing the graphitic thickness across the 0.5 mm diameter of the XPS analysis spot size on the substrate. The values found in Table 1 provide a convenient benchmark to estimate the thickness of FLG formed at different growth temperatures.

The graphene coverage for FLG samples grown with $T < 1450$ °C was not significant and therefore the XPS data cannot be used for reliable thickness calculations. In this case, the graphene thickness listed in Table 1 was inferred from coverage of graphene estimated from AFM images.

Table 1 – Summary of thickness data for FLG growth on 4H-SiC$(000\bar{1})$.

Growth temperature (°C)	Average graphene thickness from XPS (nm)	Equivalent monolayers
1350	–	~0.05[a]
1450	–	~0.1[a]
1475	1.8 ± 0.1	~5
1500	2.4 ± 0.2	~7
1550	3.7 ± 0.2	~11

[a] The average graphene coverage inferred from AFM studies.

4. AFM results

4.1. *The FLG surface as a function of growth temperature*

At growth temperatures starting from ~1350 °C, small decorated regions localized near the step-edges in the SiC substrate appear, as shown in Fig. 2(a). A height histogram

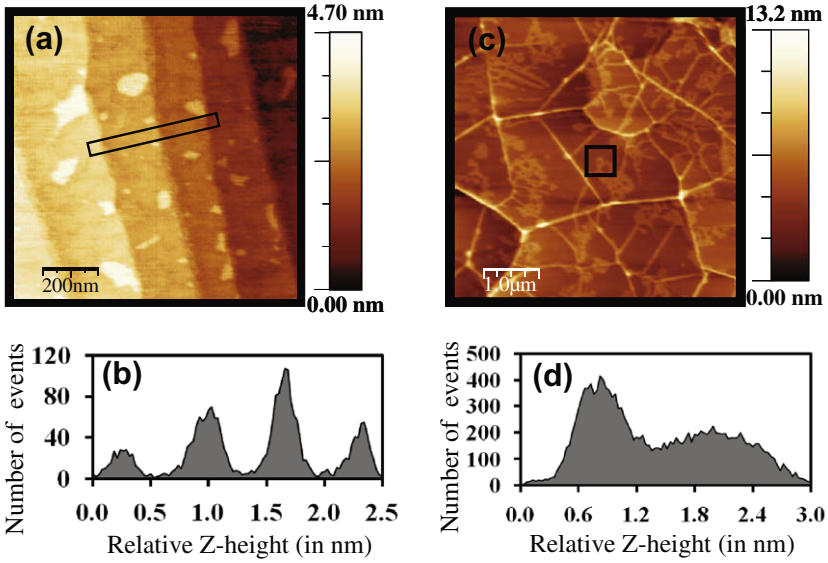

Fig. 2 – AFM images of a 4H–SiC(000$\bar{1}$) substrate. In (a), a 1 μm × 1 μm AFM image of the SiC substrate after heating for 10 min at a temperature of 1350 °C. In (b), a height histogram of the rectangular area in (a). The steps are ~0.7 nm high. In (c), a 5 μm × 5 μm AFM image of a SiC substrate after heating for 10 min at a temperature of 1475 °C. Two features that dominate the image are a mesh-like network of ridges and rough patches that decorate the flat tile-like facets. In (d), a height histogram from the rectangular area in (c). The histogram shows two well-defined peaks and indicates that the flat tile-like facets contain rough features that are, on average, ~1.2 nm in height above the flat substrate.

spanning a few of the steps in the SiC substrate is given in Fig. 2(b) and indicates the step heights are ~0.7 nm high. Further analysis of the AFM images reveal the small patches evident in Fig. 2(a) cover ~5% of the total area. As the growth temperature increases to 1450 °C, the decorations increase in size and cover ~10% of the total area (image not shown).

As indicated by the XPS results, a continuous layer of graphitic material forms at growth temperatures of 1475 °C and greater. The surface morphology that develops at 1475 °C is shown in the AFM image presented in Fig. 2(c). It is evident that the graphitic surface exhibits a meshwork of one-dimensional (1d) ridges. The ridges are not of uniform height and contain a number of localized ridge nodes where individual ridges intersect. The FLG surface bears a resemblance to a piece of crumpled paper that is subsequently unfolded and moderately smoothed.

In addition to the ridge network, Fig. 2(c) reveals a rough graphitic surface at 1475 °C. This surface is better characterized by the height histogram plotted in Fig. 2(d) that shows two broad height distributions characterizing the area enclosed by the black box in Fig. 2(c). The lower of the two peaks in this histogram is a measure of the roughness of the flatter regions on the substrate and probably reflects the intrinsic roughness of the interface layers forming on 4H–SiC(000$\bar{1}$). The right-most peak indicates the presence of features that are ~1.2 nm higher than the substrate. The broad distribution of heights evident in the right-most peak in Fig. 2(d) indicates these features further roughen the graphitic surface.

As the growth temperature is increased, the rate of sublimation of Si increases and more C atoms self-organize into FLG, causing the thickness of the graphitic layer to increase (see Table 1). Representative AFM images of FLG for 4H–SiC heated to 1500, 1525, 1550 and 1600 °C, are given in Fig. 3. These images show that the mesh-like network of ridges observed at growth temperatures of 1475 °C continues to develop for all growth temperatures studied. These ridges significantly roughen the surface of the FLG. The flat regions between the ridges become atomically flat and have been extensively characterized in parallel STM studies which show atoms arranged in a hexagonal network with a spacing of 0.245 nm [21]. At the highest growth temperature, a tent-like feature is observed as a bright white irregular-shaped polygon in Fig. 3(d). Similar features have been recently reported in carbon nanolayers deposited from the gaseous phase on Ni [26].

Apart from the mesh-like ridge network, the FLG overlayer forms flat tile-like facets that conformally coat the SiC substrate. To investigate whether features in the SiC substrate influence the ridge formation, we find that a simple derivative of an AFM image is sufficient to reveal the location of buried substrate features. Fig. 4(a) and (b) shows two typical derivative AFM images obtained from the C-face of 4H–SiC heated for ten minutes at 1500 and 1600 °C. Both images are marked in places to illustrate the underlying steps in the SiC substrate. For growth temperatures of 1500 °C, the steps are parallel to each other, a common feature observed in the as-received SiC substrates. For growth temperatures of 1600 °C, the underlying steps become rounded into well-defined plateaus. Evidence for step bunching is also present. Although occasionally a ridge is aligned along a step edge, we find no convincing evidence that step-like features in the SiC substrate seed the location of the ridge network.

Careful examination of the ridge networks observed during the course of this study indicates that the ridges can be categorized into primary and secondary ridges. The arrows in Fig. 4(a) and (b) point to primary ridges as well as a few

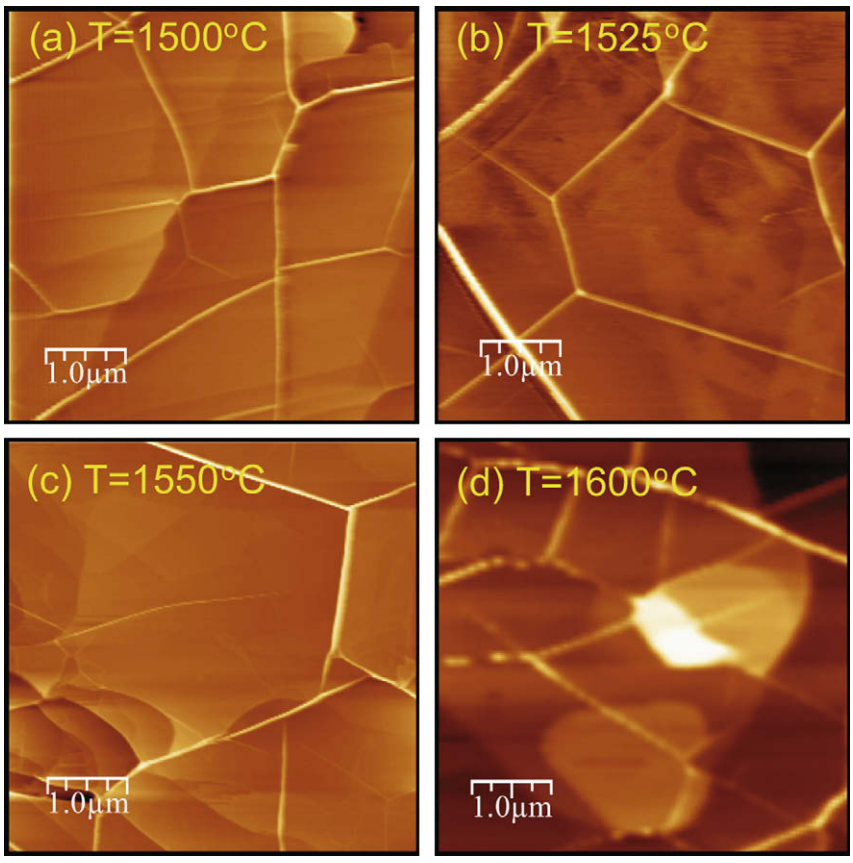

Fig. 3 – A comparison between 5 μm × 5 μm AFM images of FLG grown on 4H–SiC$(000\bar{1})$ substrate at growth temperatures of (a) T_G = 1500 °C, (b) T_G = 1525 °C, (c) T_G = 1550 °C, and (d) T_G = 1600 °C. All samples were held at the specified growth temperature for 10 min.

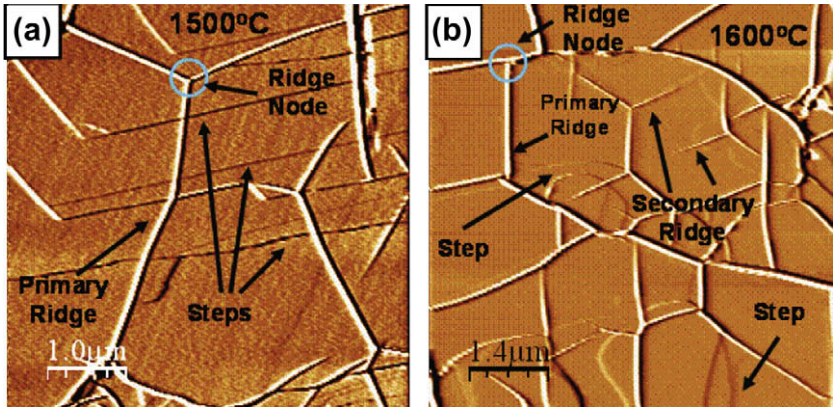

Fig. 4 – In (a), the derivative of a typical AFM image obtained from FLG grown at 1500 °C for 10 min. In (b), the derivative of a typical AFM image obtained from FLG grown at 1600 °C for 10 min.

secondary ridges. Secondary ridges often have the appearance of creases or pleats in the flat FLG facets. The distinction between a primary ridge and a secondary ridge is as follows: (i) the maximum height of a secondary ridge is typically less than the height of a primary ridge; (ii) a secondary ridge often appears to emanate from a primary ridge and forms a crease-like distortion on the surface of a flat, tile-like graphitic facet; and (iii) the height of a secondary ridge gradually decreases to zero as it merges into the flat FLG, while a primary ridge maintains a reasonably constant height between two ridge nodes. In parallel STM studies of the identical SiC samples evidence for moire' superlattices on the flat tile-like facets were found [21]. These superlattices were attributed to the relative rotation between two graphene layers.

As shown in Fig. 5(a), analysis of our AFM images show that the average height of the primary ridges increases linearly

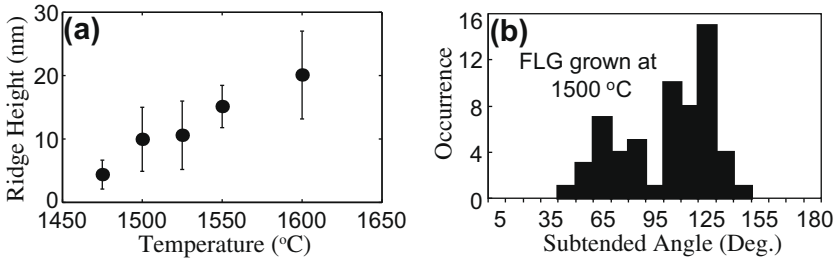

Fig. 5 – In (a), the average height of ridges in FLG samples plotted as a function of the growth temperature. In (b), a histogram plot of the subtended angle between ridges for the FLG sample grown at 1500 °C.

with growth temperature. As can be seen in Figs. 4(a) and (b), the ridges are interconnected, often diverging from a well-defined ridge node by forming a subtended angle, Θ. Studies were performed to determine if preferred values for the angle Θ could be statistically identified. A histogram of the measured angles Θ for FLG grown at 1500 °C is plotted in Fig. 5(b) and shows a preference for angles of $60 \pm 10°$ and $120 \pm 10°$. Since these angles are close to high-symmetry directions in the graphene lattice, we infer that ridge formation tends to occur along high-symmetry directions in the FLG film.

4.2. *Thermal contraction on the carbon face of 4H–SiC*

The common occurrence of a mesh-like network of ridges in FLG grown at elevated temperatures suggests the origin of ridge formation might be related to thermal-induced buckling of FLG due to stress generated by cooling. A difference in thermal contraction between the SiC substrate and the FLG overlayer is sufficient to produce the required stress. Local deformation (delamination) of the FLG can occur if there is detachment between the FLG and the underlying SiC due to sufficiently weak bonding. To investigate this idea further, accurate values for the thermal expansion of graphene and SiC are required. We are not aware of measurements for the thermal contraction of FLG [27], but the thermal contraction for graphite has been experimentally studied for over 40 years because of its widespread use in nuclear reactors. This highly anisotropic material is characterized by a specific temperature (~393 °C) at which the thermal expansion equals zero.

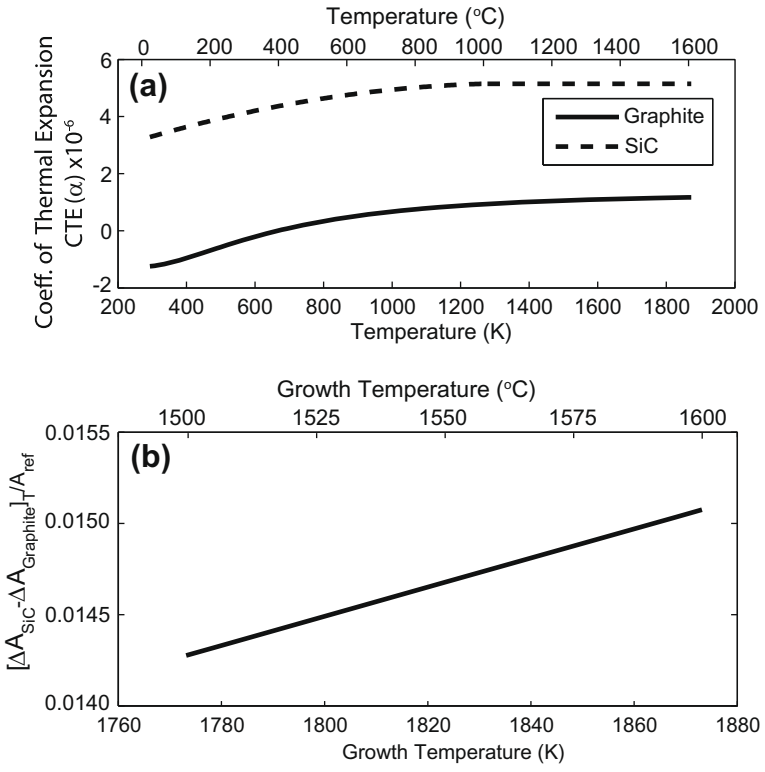

Fig. 6 – In (a), the coefficient of thermal expansion of the basal plane of 4H–SiC$(000\bar{1})$ (dashed line, Ref. [32]) and the basal plane of graphite (solid line, Ref. [31]). For temperatures greater than 1000 °C the coefficient of thermal expansion of 4H–SiC is assumed to be constant. In (b), the predicted fractional change in area between SiC and graphite when cooled from a specific growth temperature to room temperature (20 °C).

The basal and c-axes values of the coefficient of thermal expansion (CTE) for graphite have been measured [28] and a set of thermodynamic equations have been developed [29]. The values given by Morgan [30] are used in what follows because they provide a better estimate to the experimental data at higher temperatures and also correctly predict that CTE = 0 at 393.6 °C [28,31]. The thermal expansion for 4H–SiC in the range of 20–1000 °C is described by a second-order polynomial equation [32]. Plots of the coefficient of thermal expansion as a function of temperature for the basal plane for graphite and 4H–SiC are given in Fig. 6(a). Values of CTE for 4H–SiC(α_{SiC}) beyond 1000 °C could not be found in the literature. In what follows, we approximated α_{SiC} for $T > 1000$ °C by a constant as shown in Fig. 6(a).

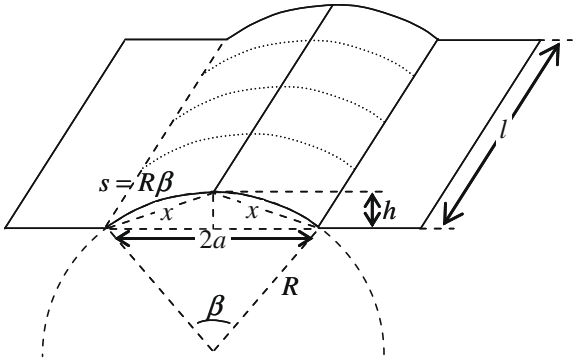

Fig. 7 – Schematic of a ridge structure showing the relevant parameters for estimating the excess area.

Using these literature values, the fractional change in area ($\Delta A/A_{ref}$) between a SiC substrate and a FLG film grown at a temperature T after cooling to a reference temperature (T_0 = room temperature, 20 °C) can be calculated by

$$\frac{\Delta A}{A_{ref}} \equiv \frac{\left[\Delta A_{SiC} - \Delta A_{graphite}\right]_T}{A_{ref}} = 2\int_T^{T_{ref}} \left[\alpha_{SiC} - \alpha_{graphite}\right] dT \qquad (7)$$

Eq. (7) can be evaluated numerically using the data plotted in Fig. 6(a). The fractional change in area for cooling from 1475 °C < T < 1600 °C to 20 °C is plotted in Fig. 6(b).

It is useful to estimate the excess area experimentally observed, since it can be compared to the results plotted in Fig. 6(b). The excess area in a given AFM scan can be estimated by summing the excess area contained in individual ridges. A schematic of a ridge is shown in Fig. 7. Assuming, there are N ridges in a scan having an area A_0, the excess area ΔA due to the formation of ridges is given as:

$$\Delta A = \sum_{i=1}^{N} (s_i - 2a_i) l_i \qquad (8)$$

where s_i, $2a_i$ and l_i represent the arc length, chord length and the length of individual ridges, respectively. For small subtended angles β_i, the arc length s_i can be approximated as $2x_i$. The excess area is then given by

$$\Delta A \cong \sum_{i=1}^{N} (2x_i - 2a_i) l_i = \sum_{i=1}^{N} 2l_i \left[(a_i^2 + h_i^2)^{1/2} - a_i \right] \cong \sum_{i=1}^{N} \frac{l_i h_i^2}{a_i} \qquad (9)$$

Eq. (9) can be evaluated from AFM images by straightforward measurements of the ridge dimensions.

Estimates of the excess fractional area contained in the ridges from representative AFM images give values that are about 1/10 of those plotted in Fig. 6(b). The discrepancy

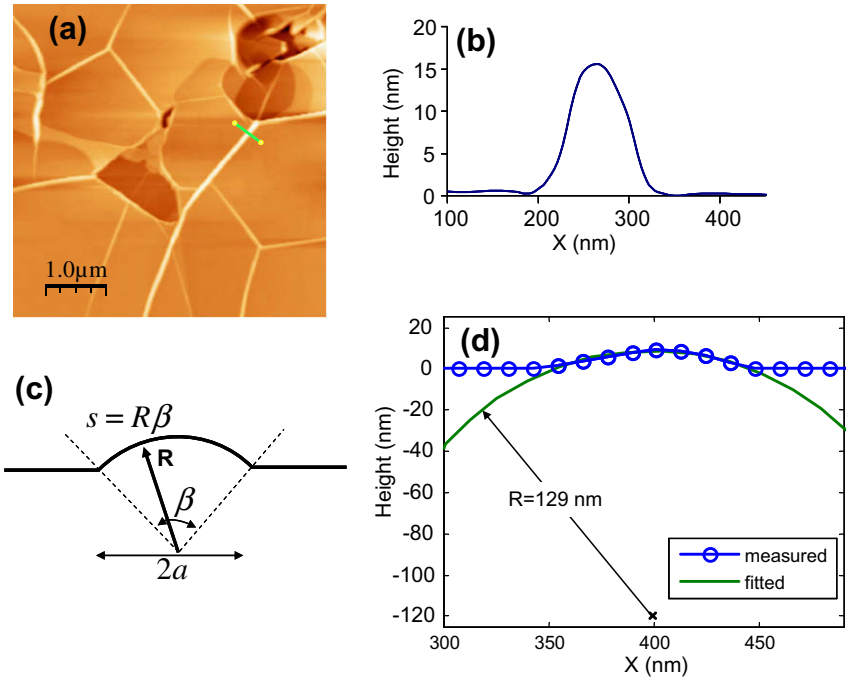

Fig. 8 – In (a), an AFM image of primary ridges on FLG grown at 1550 °C on 4H–SiC. In (b), the cross-sectional line profile along the line in (a). In (c), a schematic cross-section of a ridge of width 2*a*. In (d), the results of a least-squares fit of the ridge profile to a circle. The radius of curvature of the ridge is found to be 129 nm.

between calculation and experiment might indicate the presence of localized regions in the FLG that are severely deformed or that the graphene–SiC interface can slip, greatly reducing the number of ridges that are formed.

4.3. *Strain in primary and secondary ridges*

From typical AFM images (Fig. 8(a)), it is possible to define a strain parameter for the top graphene layer forming the ridge network. The procedure is illustrated in Fig. 8(c) which shows a schematic diagram of a cross-sectional profile of a ridge of width $2a$. The strain parameter ε is defined as,

$$\varepsilon = \frac{\Delta\ell}{\ell} = \frac{s - 2a}{2a} \tag{10}$$

where s is the length of the ridge arc and $2a$ is the width at the base of the ridge. Fig. 8(a) is an AFM image of a ridge network found in an FLG sample grown at 1550 °C on 4H–SiC$(000\bar{1})$. Fig. 8(b) shows the height cross-section of the primary ridge indicated in Fig. 8(a). Using this contour shape, a least-squares fit to a circle can be performed to determine the arc length s that appears in Eq. (10). The resulting fit is shown in Fig. 8(d) and gives $R \approx 129$ nm. From this information, we estimate that ε for this ridge is about 0.044. Calculations (not shown) indicate the error in ε due to tip-sample dilation when the typical tip radius is assumed to be 2 nm is negligible. For tip radii of ~5 nm, the error in ε is estimated to be about −2.7%.

A similar strain analysis was performed along a typical secondary ridge from an FLG sample grown at 1550 °C on 4H–SiC. The results, shown in Fig. 9 as a function of distance from the free end of the ridge, indicate that the maximum strain in a secondary ridge is typically smaller than that found in primary ridges. Furthermore, a least-squares fit to the strain in Fig. 9 indicates that the strain vanishes quadratically with length from the ridge end, going to zero when the secondary ridge merges smoothly into the FLG surface. The strain estimates for both primary and secondary ridges neglect the curvature along the length of a ridge which is small when compared to the curvature in the direction perpendicular to the ridge.

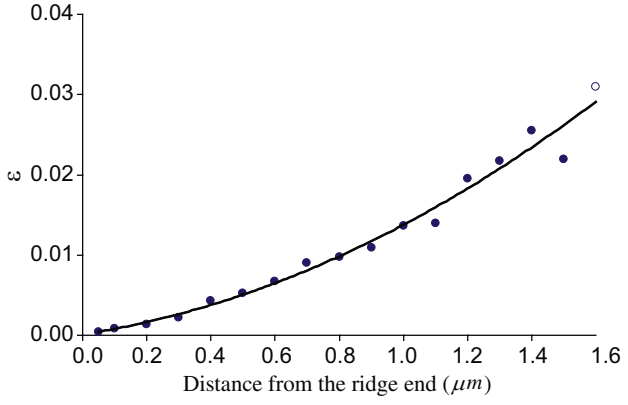

Fig. 9 – The strain in a secondary ridge of an FLG sample grown at 1550 °C on 4H–SiC as a function of length. The solid line is the result of a least-squares fit.

5. Discussion

As determined from the AFM studies discussed above, the graphitic layer that forms on the surface of the C-face of 4H–SiC contains flat tile-like regions of FLG surrounded by a highly deformed, 1d ridge-like mesh network. Parallel XPS studies confirm the growth of a thin graphitic layer on 4H–SiC$(000\bar{1})$ that increases in thickness as the growth temperature increases. The first step in eliminating this 1d ridge-like network is to identify the relevant factors that cause a coarsening of the graphitic surface layer in this characteristic way.

Upon cooling, anisotropic compressive stress develops due to the differential thermal contraction between SiC and the graphitic overlayer. In response to this compressive stress, the FLG film deforms and buckles, forming ridges upon cooling. At this time, we do not conclusively know whether this buckling occurs due to intrinsic corrugation fluctuations or rippling in the graphene layers [33] or whether it is seeded by point-like defects in the FLG that form during graphene growth. Localized height protrusions, typically observed at ridge nodes, suggest that ridge formation is seeded from well-defined point-like defects. Likely candidates for such defects in the graphene lattice are pentagonal defects [34,35], sharp kinks in grain boundaries [21], or 5-8-5 vacancies (di-vacancies) [36].

Stoichiometric considerations offer a possible explanation for the formation of such defects. While both graphene and SiC have hexagonal unit cells, the lattice mismatch produces a deficit of available carbon atoms from the evaporation of only a single Si layer. In one bilayer of SiC, there are 12.2 carbon atoms/nm^2. To form one layer of graphene, 38.2 carbon atoms/nm^2 are required. To free enough carbon atoms to form a continuous layer of graphene, the sublimation of more than three bilayers of SiC is required [22,37,38].

After mobile carbon atoms organize to form FLG at high temperatures, compressive stress builds upon cooling. Since the bending rigidity of thin plates tends to be generally smaller than their stretching rigidity, buckling of the FLG can occur as a result of the complex stress patterns that develop.

Initially, a wrinkling is expected to occur in the FLG thin film membrane. The amplitude of these compressive-induced wrinkles is a problem of general interest and has been discussed in the much broader context of scaling laws to better characterize the mechanical properties of compressed thin solid membranes [39–42]. As the stress increases, the wavelength of the wrinkles decreases until a wrinkle-to-fold transition occurs [43]. This transition is thought to be universally applicable to a broad class of diverse membrane systems [44–49] which exhibit advanced functionality based on the formation of folds from wrinkles. We expect a similar process will occur in FLG grown epitaxially on a solid substrate at high temperatures.

The driving force for the formation of ridges (or folds) is the minimization of the strain energy in the FLG film. Ridges form during cool down when wrinkles coalesce. The ridges likely align themselves in directions determined by the weakest points in the FLG film, in much the same way that cracks propagate following directions of least resistance. A statistical study of the ridge orientation (see Fig. 5(b)) provides evidence that many of the ridges meet at points subtended by angles

that match the underlying symmetry of the graphene lattice. However, a significant number of ridges do not follow this trend and it is likely that the orientation of these ridges is largely determined by random defects in the FLG.

We observe two different types of ridges. Primary ridges have a height that increases with the thickness of FLG. The primary ridges are interconnected at ridge nodal points and emanate outward, often forming a threefold crease-like pattern in FLG. In contrast to the primary ridges, which often have a nearly constant height over distances spanning micrometers, secondary ridges also develop. Secondary ridges are distinguished by a diminishing height that smoothly goes to zero, producing a 1d distortion that eventually disappears into the flat FLG surface. The formation of the primary and secondary ridges is the likely cause of the rotation between two graphene layers that produce a moire' superlattice in the flat, tile-like FLG [21].

The Euler buckling instability for thin membranes has been extensively discussed [39–42,50] and extended to single layered graphene [51] and coupled nano-layers [52]. Of interest within the context of FLG growth is the theoretical expectation that the ratio of surface roughness (height of ridges) to the linear size of the flat tile-like facets should scale as the square root of the externally imposed strain [50].

There are claims in the literature that ridge features similar to those studied here are really nanotubes/nanorods that form during graphene growth on the SiC surface [53–55]. While the appearance of such nanotubes/nanorods oriented perpendicular to the substrate can be easily identified, it is difficult to understand how nanotube growth can take place parallel to the substrate. Furthermore it is hard to understand why the nanotubes/nanorods would tend to arrange with subtended angles near 60° or 120° as found in Fig. 5(b). Lastly, one might expect that a nanotube/nanorod feature resting on a substrate would have an approximate circular cross-section. However, we find that measurements of the height-to-width ratio of ridges imaged in this study are much less than unity, even after tip dilation with an AFM tip radius between 2 and 5 nm. This indicates the ridges are far from having a circular cross-section that might be expected for nanotubes. Taken together, these arguments suggest that the 1d ridge-like features bear little resemblance to nanotubes or nanorods that rest on a substrate.

Due to the high radius of curvature characterizing the ridges, elastic strain energy becomes concentrated in the mesh-like network. As discussed above, by measuring the radius of curvature of a line profile from a ridge, it is possible to quantitatively estimate the strain involved. Accordingly, ridge formation might be suppressed by increasing the bending rigidity of FLG as the thickness of the FLG increases. According to thin plate theory, the bending rigidity D of a free-standing plate is given by

$$D = \frac{Et^3}{12(1-\nu^2)} \tag{11}$$

where E is Young's modulus (in the plane of the plate), t is the thickness of the plate, and ν is Poisson's ratio. For a layered material like FLG, one might expect slippage between graphene layers to further reduce D below the value predicted by Eq. (11). Alternatively, since the FLG under study is supported by a SiC substrate, the bending rigidity might be further increased beyond the free-standing value depending on the mechanical coupling between the FLG and the SiC substrate.

Recent experiments [56] find that $D \approx 1\text{–}2 \times 10^{-15}$ J for free standing FLG that is only 1–2 nm thick. Evidently, the t^3 dependence on thickness in Eq. (8) adequately estimates D, even though the side-length to thickness ratio of the FLG is typically much greater than 100. Using these estimates for D in FLG, at growth temperatures near 1500 °C, $k_B T \ll D$, suggesting that thermal fluctuations alone are insufficient to initiate any significant bending.

Using the results given in Table 1, we can estimate that the bending rigidity of FLG grown at 1475 and 1550 °C should increase by roughly a factor of 9 based on thickness considerations alone. However, a factor of 9 increase in bending rigidity does not suppress the ridges that form. In fact, the opposite seems to be true. We conclude that arguments based on thin plate theory alone are not able to account for our observations of ridge formation in FLG.

The features discussed in this manuscript have been observed by many research groups working on graphite. High dose carbon-bombardment on graphite produces ridges and tiles [57]. Ridge formation has been attributed to carbon atom transport by diffusion from heavily damaged near-surface regions or by a tectonic-plate-like motion or both. Graphite surfaces after oblique single-ion impact revealed hillocks that decorate the surface [58]. The accumulation of carbon interstitials between the graphitic layers accounted for the hillock formation. A mechanism of subsurface damage in the form of interstitial accumulation along ion-tracks which cause an expansion of the lattice along the c-axis has also been suggested [59]. Taken together, these prior studies emphasize the importance of interstitial carbon atoms in ridge formation.

6. Conclusions

Hydrogen-etched 4H–SiC$(000\bar{1})$ substrates were held at elevated temperatures under high vacuum conditions for ten minutes. After cooling to room temperature, systematic studies of the graphitic material on the C-face of the SiC substrates as a function of growth temperature were performed. For growth temperatures near 1350 °C, AFM images showed localized features that primarily decorated the step edges of SiC. No continuous layer of graphitic carbon was observed. XPS studies of 4H–SiC$(000\bar{1})$ samples heated to temperatures greater than 1450 °C confirmed the presence of a graphitic layer; the thickness of this graphitic layer increased with growth temperature.

AFM studies of the C-face of the 4H–SiC surface subjected to temperatures greater than 1450 °C revealed micron-sized flat areas of graphene coating the SiC substrate, irrespective of underlying step edges and plateaus present in the substrate. An interlocking mesh of ridge-like features was found to border the tile-like regions of atomically flat FLG for every sample studied. The ridge network serves to roughen the surface of FLG in an uncontrolled way for all growth temperatures above 1475 °C.

The origin of the ridge-like network is attributed to the 2d compressive stresses that develop upon cooling from the growth temperature. The precise shape of the ridge-like

network is driven by intrinsic buckling instabilities of the FLG and is likely influenced by the random location of atomic-scale point-like defects that form during graphene growth. Both primary and secondary ridges have been identified and studied. From the cross-sectional geometry of the ridge network, quantitative estimates for the strain at any point along the ridge can be obtained. The presence of a ridge network conclusively demonstrates that the stored elastic energy is inhomogeneously distributed in FLG.

In order to reduce the ridge network, the coupling between the SiC substrate and the FLG layer must be reduced, possibly by the growth of a suitably designed intermediate coupling layer. Alternatively, the SiC substrate could be pre-patterned into smaller plateaus that are effective in relieving the stress that develops upon cooling.

Acknowledgements

The authors would like to thank L. Biedermann, J. Cooper, J. Appenzeller and T. Sands for helpful comments during the course of this work. The work was supported in part by the Indiana 21st Century Fund and DARPA.

REFERENCES

[1] Katsnelson MI. Graphene: carbon in two dimensions. Mater Today 2007;10(1–2):20–7.
[2] Neto AHC, Guinea F, Peres NMR, Novoselov KS, Geim AK. The electronic properties of graphene. Rev Mod Phys 2009;81(1):109–62.
[3] Novoselov KS, Geim AK, Morozov SV, Jiang D, Zhang Y, Dubonos SV, et al. Electric field effect in atomically thin carbon films. Science 2004;306(5696):666–9.
[4] Chen Z, Lin Y-M, Rooks MJ, Avouris P. Graphene nano-ribbon electronics. Phys E: Low-Dimens Syst Nanostruct 2007;40(2):228–32.
[5] Li X, Wang X, Zhang L, Lee S, Dai H. Chemically derived, ultrasmooth graphene nanoribbon semiconductors. Science 2008;319:1229–32.
[6] Wu YQ, Ye PD, Capano MA, Xuan Y, Sui Y, Qi M, et al. Top-gated graphene field-effect-transistors formed by decomposition of SiC. Appl Phys Lett 2008;92(9):092102-3.
[7] Huard B, Sulpizio JA, Stander N, Todd K, Yang B, Goldhaber-Gordon D. Transport measurements across a tunable potential barrier in graphene. Phys Rev Lett 2007;98(23):236803-4.
[8] Lin Y-M, Jenkins KA, Valdes-Garcia A, Small JP, Farmer DB, Avouris P. Operation of graphene transistors at gigahertz frequencies. Nano Lett 2008;9(1):422–6.
[9] Berger C, Song Z, Li X, Wu X, Brown N, Naud C, et al. Electronic confinement and coherence in patterned epitaxial graphene. Science 2006;312:1191–6.
[10] Zhang Y, Tan Y-W, Stormer HL, Kim P. Experimental observation of the quantum Hall effect and Berry's phase in graphene. Nature 2005;438(7065):201–4.
[11] Liang X, Fu Z, Chou S. Graphene transistors fabricated via transfer-printing in device active-areas on large wafer. NanoLett 2007;7:3840–4.
[12] Forbeaux I, Themlin JM, Debever JM. Heteroepitaxial graphite on 6H–SiC(0 0 0 1): interface formation through conduction-band electronic structure. Phys Rev B 1998;58:16396–406.
[13] Angot T, Portail M, Forbeaux I, Layet JM. Graphitization of the 6H–SiC(0 0 0 1) surface studied by HREELS. Surf Sci 2002;502–503:81–5.
[14] Taisuke O, Farid El G, Aaron B, Jessica LM, Konstantin VE, Andreas KS, et al. Morphology of graphene thin film growth on SiC(0 0 0 1). New J Phys 2008(2):023034-7.
[15] Hannon JB, Tromp RM. Pit formation during graphene synthesis on SiC(0 0 0 1): in situ electron microscopy. Phys Rev B (Condens Matter Mater Phys) 2008;77(24):241404-4.
[16] Emtsev KV, Seyller T, Speck F, Ley L, Stojanov P, Riley JD, et al. Initial stages of the graphite–SiC(0 0 0 1) interface formation studied by photoelectron spectroscopy. Mater Sci Forum 2006;525:556–7.
[17] Starke U. Reconstruction and epitaxial adlayers on SiC surfaces: structural significance for technological applications. Mat Res Symp 2003;742:K1.5.1–K1.5.11.
[18] Ferrari AC, Meyer JC, Scardaci V, Casiraghi C, Lazzeri M, Mauri F, et al. Raman spectrum of graphene and graphene layers. Phys Rev Lett 2006;97(18):187401-4.
[19] Gupta A, Chen G, Joshi P, Tadigadapa S, Eklund PC. Raman scattering from high-frequency phonons in supported n-graphene layer films. Nano Lett 2006;6(12):2667–73.
[20] Jeong S-K, Inaba M, Iriyama Y, Abe T, Ogumi Z. AFM study of surface film formation on a composite graphite electrode in lithium-ion batteries. J Power Sources 2003;119–121:555–60.
[21] Biedermann LB, Bolen ML, Capano MA, Zemlyanov D, Reifenberger RG. Insights into few-layer epitaxial graphene growth on 4H–SiC(000$\bar{1}$) substrates from STM studies. Phys Rev B (Condens Matter Mater Phys) 2009;79(12):125411-10.
[22] Chao T, Lijun M, Huaping X, Jianxin Z. Growth of graphene structure on 6H–SiC(0 0 0 1): molecular dynamics simulation. J Appl Phys 2008;103(6):063505-5.
[23] Horcas I, Fernandez R, Gomez-Rodriguez JM, Colchero J, Gomez-Herrero J, Baro AM. WSXM: a software for scanning probe microscopy and a tool for nanotechnology. Rev Sci Instrum 2007;78(1):013705–8.
[24] Fadley CS. Basic concepts of X-ray photoelectron spectroscopy. Electron spectroscopy: theory, techniques, and applications, vol. 2. New York: Academic Press Inc.; 1978.
[25] NIST SRD-82. National institute of standards and technology. Gaithersburg, MD; 2001.
[26] Nyapshaev I, Makarenko I, Titkov A, Tyurnina A, Obraztsov A. Structural peculiarities of carbon nanolayers prepared by deposition from a gaseous phase on Ni. Phys Solid State 2009;51(5):1054-9.
[27] The CTE for a single layer graphene has been calculated using *ab initio* methods. See Nicolas M, Nicola M. First-principles determination of the structural, vibrational and thermodynamic properties of diamond, graphite, and derivatives. Phys Rev B (Condens Matter Mater Sci) 2005;71:205214.
[28] Steward EG, Cook BP, Kellett EA. Dependence on temperature of the interlayer spacing in carbons of different graphitic perfection. Nature 1960;187(4742):1015–6.
[29] Riley DP. The thermal expansion of graphite: part II. Theor Proc Phys Soc 1945;1(6):486–95.
[30] Morgan WC. Thermal expansion coefficients of graphite crystals. BNWL-SA-3838; 1971.
[31] Tsang DKL, Marsden BJ, Fok SL, Hall G. Graphite thermal expansion relationship for different temperature ranges. Carbon 2005;43(14):2902–6.
[32] Li Z, Bradt RC. Thermal expansion of the hexagonal (4H) polytype of SiC. J Appl Phys 1986;60(2):612–4.
[33] Fasolino A, Los JH, Katsnelson MI. Intrinsic ripples in graphene. Nat Mater 2007;6(11):858–61.
[34] Cortijo A, Vozmediano MAH. A cosmological model for corrugated graphene sheets. Eur Phys J Spec Top 2007;148:83–9.

[35] Meyer JC, Kisielowski C, Erni R, Rossell MD, Crommie MF, Zettl A. Direct imaging of lattice atoms and topological defects in graphene membranes. NanoLett 2008;8:3582–6.
[36] Yamashita K, Saito M, Oda T. Atomic geometry and stability of mono-, di-, and trivacancies in graphene. Jpn J Appl Phys 2006;45:6534–6.
[37] Hass J, Varchon F, Millan-Otoya JE, Sprinkle M, Sharma N, de Heer WA, et al. Why multilayer graphene on 4H–SiC(000$\bar{1}$) behaves like a single sheet of graphene. Phys Rev Lett 2008;100(12):125504-4.
[38] Lauffer P, Emstev KV, Graupner P, Seyller T, Ley L, Reshanov SA, et al. Atomic and electronic structure of few-layer graphene on SiC(0 0 0 1) studied with scanning tunneling microscopy and spectroscopy. Phys Rev B 2008;77:155426–36.
[39] Moldovan D, Golubovic L. Tethered membranes far from equilibrium: buckling dynamics. Phys Rev E 1999;60(4): 4377–84.
[40] Moldovan D, Golubovic L. Buckling dynamics of compressed thin sheets (membranes). Phys Rev Lett 1999;82(14):2884–7.
[41] Cerda E, Ravi-Chandar K, Mahadevan L. Thin films: wrinkling of an elastic sheet under tension. Nature 2002;419(6907):579–80.
[42] Cerda E, Mahadevan L. Geometry and physics of wrinkling. Phys Rev Lett 2003;90:074-302-4.
[43] Pocivavsek L, Dellsy R, Kern A, Johnson S, Lin B, Lee KYC, et al. Stress and fold localization in thin elastic membranes. Science 2008;320(5878):912–6.
[44] Diamant H, Witten TA, Ege C, Gopal A, Lee KYC. Topography and instability of monolayers near domain boundaries. Phys Rev E 2001;63(6):061602-12.
[45] Gopal A, Lee KYC. Morphology and collapse transitions in binary phospholipid monolayers. J Phys Chem B 2001;105(42): 10348–54.
[46] Collier CP, Vossmeyer T, Heath JR. Nanocrystal superlattices. Annu Rev Phys Chem 1998;49(1):371–404.
[47] Mueggenburg KE, Lin X-M, Goldsmith RH, Jaeger HM. Elastic membranes of close-packed nanoparticle arrays. Nat Mater 2007;6(9):656–60.
[48] Brochard-Wyart F, de Gennes PG. How soft skin wrinkles. Science 2003;300(5618):441-1.
[49] Zasadzinski JA, Ding J, Warriner HE, Bringezu F, Waring AJ. The physics and physiology of lung surfactants. Curr Opin Colloid Interface Sci 2001;6(5–6):506–13.
[50] Golubovic L, Moldovan D, Peredera A. Dynamics of the Euler buckling instability. Phys Rev Lett 1998;81(16): 3387–90.
[51] Sakhaee-Pour A. Elastic buckling of single-layered graphene sheet. Comput Mater Sci 2009;45(2):266–70.
[52] Quinn DD, Wilber JP, Clemons CB, Young GW, Buldum A. Buckling instabilites in coupled nano-layers. Int J Non-Linear Mech 2007;42:681–9.
[53] Hayashi K, Mizuno S, Tanaka S, Toyoda H, Tochihara H, Suemune I. Nucleation stages of carbon nanotubes on SiC(0 0 0 1) by surface decomposition. Jpn J Appl Phys 2005;44:L803–5.
[54] Varchon F, Mallet P, Magaud L, Veuillen J-Y. Rotational disorder in few-layer graphene films on 6H–SiC(000$\bar{1}$): a scanning tunneling microscopy study. Phys Rev B 2008;77(16):165415-5.
[55] Naitoh M, Kitada M, Nishigaki S, Toyama N, Shoji F. An STM observation of the initial process of graphitization at the [formula] surface. Surf Rev Lett 2003;10(2/3):473–7.
[56] Poot M, van der Zant HSJ. Nanomechanical properties of few-layer graphene membranes. Appl Phys Lett 2008;92(6):063111-3.
[57] Annis BK, Pedraza DF, Withrow SP. Topographical changes induced by high dose carbon-bombardment of graphite. J Mater Res 1993;8(10):2587–99.
[58] Reimann KP, Bolse W, Geyer U, Lieb KP. Atomically resolved imaging of the defect structure on graphite after oblique single-ion impact. Europhys Lett 1995;30:463–8.
[59] Porte L, de Villeneuve CH, Phaner M. Scanning tunneling microscopy observation of local damages induced on graphite surface by ion implantation. AVS; 1991. p. 1064–7.